Research in Astronomy and Astrophysics, 22:105003 (15pp), 2022 October https://doi.org/10.1088/1674-4527/ac8b5a

Faint Space Debris Detection Algorithm Based on Small Aperture Telescope Detection System

Ping Jiang[1,2], Chengzhi Liu[1,2,3], Zhe Kang[1,2], Wenbo Yang[1,2], and Zhenwei Li[1,2]
[1] Changchun Observatory of National Astronomical Observatories, Chinese Academy of Sciences, Changchun 130117, China; lcz@cho.ac.cn
[2] University of Chinese Academy of Sciences, Beijing 100049, China
[3] Key Laboratory of Space Object & Debris Observation, PMO, CAS, Nanjing 210008, China
Received 2022 March 29; revised 2022 July 11; accepted 2022 August 12; published 2022 September 16

Abstract

Ground-based optical observation has unique advantages in space target observation. However, due to the weak light-gathering ability of small-aperture optoelectronic observation telescopes, the space debris in the image is weak and easily drowned in noise. In order to solve the above problems, we use digital image processing technology to extract faint space debris. We propose a high detection rate space debris automatic extraction algorithm, aiming to automatically detect space debris. We first establish a new space target description model. Our algorithm is mainly divided into two stages. The purpose of the first stage is to reduce the influence of a large number of stars. We perform wavelet transform and guided filtering for three consecutive frames, and the reconstructed wavelet that takes the median value can achieve the effect of eliminating stars. In the second stage, we adopt the method of robust principal component analysis and attribute the problem of target detection to the problem of separating the target and background of a single frame of image. After a large number of experimental results analysis, it is proved that the algorithm can effectively detect faint debris in the monitoring system of small aperture telescope, and has high precision and low computational complexity.

Key words: instrumentation: detectors – methods: data analysis – methods: observational

1. Introduction

Space targets mainly refer to artificial satellites, and also include various space debris, such as booster rockets, protective shields and other objects entering the space orbit, as well as various space flying objects entering the outer space of the earth. Space target detection is the process of searching and positioning space targets based on the captured sequence star image (Schildknecht 2007). This technology can not only help us understand the outer space of the earth, but also will occupy a very important position in future space offenses and defenses (Du et al. 2016).

For a long time, the detection of space debris under complex background has always been a hot research topic. Since both the target and the background star are similar to point target imaging, it is difficult to distinguish the target and the background star by using the visual characteristics of the target grayscale feature, regional feature, shape, color and texture, as shown in Figure 1 (Figure 1(a) shows the physical image of the observatory space probe telescope. Figures 1(b)–(d) are real astronomical images). Therefore, many methods have been proposed to solve the problem of faint target detection in optical images. For example, template matching method (Liu et al. 2012; Murphy et al. 2016), morphological operator (Wei et al. 2018), neural network (Jia et al. 2020). Jiao proposed a method of combining high-level statistics and prediction. Using background prediction, the noise in the image can be better removed and the accurate prediction of the background can be achieved. Then the accurate small target image is obtained, which improves the detection accuracy (Jiao & Lingda 2017). Wang et al. proposed a nonnegativity-constrained variational mode decomposition method, which is based on traditional frequency domain filtering to separate high and low frequency targets from the background. The method can adaptively decompose the input signal into multiple discrete band-limited sub-signals with non-negativity constraints. However, the computational complexity of the algorithm is high, which affects practical applications (Wang et al. 2017).

According to the priori motion information of the target, Yanagisawa et al. extracted the target with low signal-to-noise ratio from the median image of the sequence frame (Yanagisawa et al. 2012). Nunez et al. proposed an image deconvolution method based on Richards-luck, which is an iterative algorithm that tends to the maximum likelihood solution (Nunez et al. 2015). Sun et al. proposed a point target extraction algorithm based on mathematical morphology processing and multi-frame median filtering (Sun & Zhao 2013; Sun et al. 2015). Schildknecht et al. proposed a method by controlling the observation mode of the telescope, so that the target in the image sequence is a point image with displacement, the star is a dotted line, and the position is unchanged,

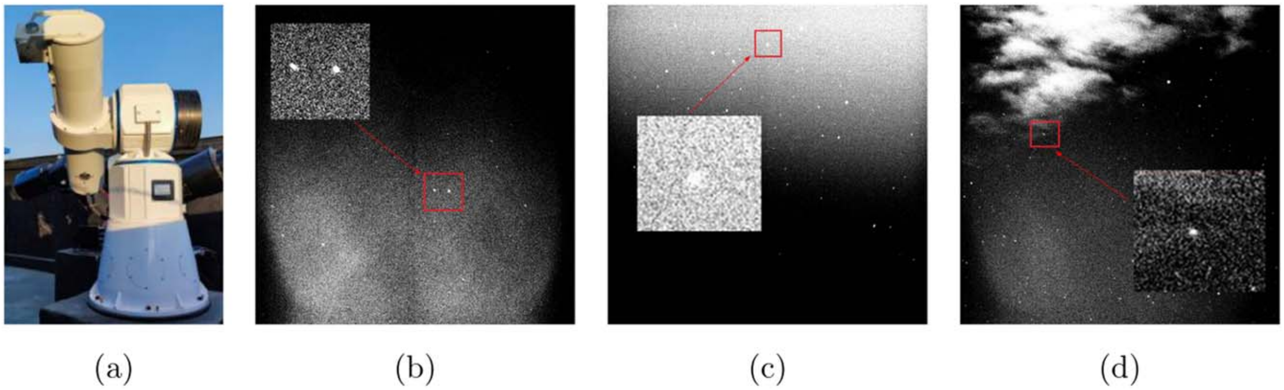

Figure 1. The original image captured by the astronomical telescope. (a) Space probe telescope components. (b)–(d) Original images captured by the astronomical telescope.

and a mask algorithm is used to filter out the background stars (Schildknecht et al. 2004). Xi et al. proposed a time-exponential filtering and bright star enhancement method, which effectively removed the stars and noise, and then obtained the real target trajectory through multi-level hypothesis testing (Xi et al. 2015).

Our algorithm focuses on faint target detection systems for small aperture telescopes, and no additional information is applied. There is also no increase in exposure time. We divide the target detection process into two parts. It is called the star removal stage and the target detection stage. The mixed filtering of wavelet transform and guided filtering is performed on the continuous three frames of images, and the median value of the three frames of images after wavelet reconstruction is taken for processing. The second stage uses the non-local autocorrelation of the background to transform the target detection into optimization problems of low-rank matrix and sparse matrix. The algorithm can have good target detection capabilities.

The structure of this paper is as follows: Section 1 introduces our research background; Section 2 describes the image processing channel in detail; Section 3 conducts data analysis and experiments; in Section 4 we draw conclusions.

2. Image Processing Channel

The astronomical telescope is in target tracking mode, the telescope moves with the target, the stars are in motion, and the target is relatively stationary in the image frame. When the exposure time is 50 ms, the stars, noise and targets are displayed as point sources. We propose a new detection strategy and divide the detection algorithm into two parts. Since the imaging mode of the telescope is the target tracking mode, it is assumed that the target and noise are static, and the stars are continuously moving. This phase is called the stellar elimination phase. The modeling is as follows:

$$F(x, y, k) = H(x, y, k) + D(x, y, k) \tag{1}$$

Here (x, y, k) represents the pixel coordinates in the star map. $F(x, y, k)$ represents the gray value of the image. $H(x, y, k)$ represents the star gray value of the image. $D(x, y, k)$ represents the background gray value of this stage. k indicates the frame number of the image. At this stage, we proposed a new star removal method, which can eliminate stars and part of the noise.

In the second stage, the image contains the target and noise, so this stage mainly separates the target. We call the second stage target detection. Figure 2 is the image processed in the star removal stage, and Figure 2(b) is the estimated background image. From the characteristics of the image in Figure 2(c), it can be known that the images in the second stage are mainly targets and noise. Its formula is as follows:

$$D(x, y, k) = T(x, y, k) + B(x, y, k) \tag{2}$$

$T(x, y, k)$ represents the target gray value of the image. $B(x, y, k)$ represents the background gray value of the image, including noise and uneven sky background (Sun et al. 2019; Castronuovo 2011). Figure 3 shows the overall structure of the algorithm.

2.1. Stellar Point Removal Stage

The astronomical images contain a lot of noise, and the target size is small. Both the target and the background stars are similar to point sources. It is difficult to distinguish the target and the background star by using the visual characteristics of the target grayscale feature, regional feature, shape and texture. Figure 4 is a schematic diagram of the processing of a single frame image. We apply the schematic diagram of Figure 4 to three continuous frames to obtain the corresponding image components. We perform edge-preserving and denoising for each component through guided filtering, and finally perform

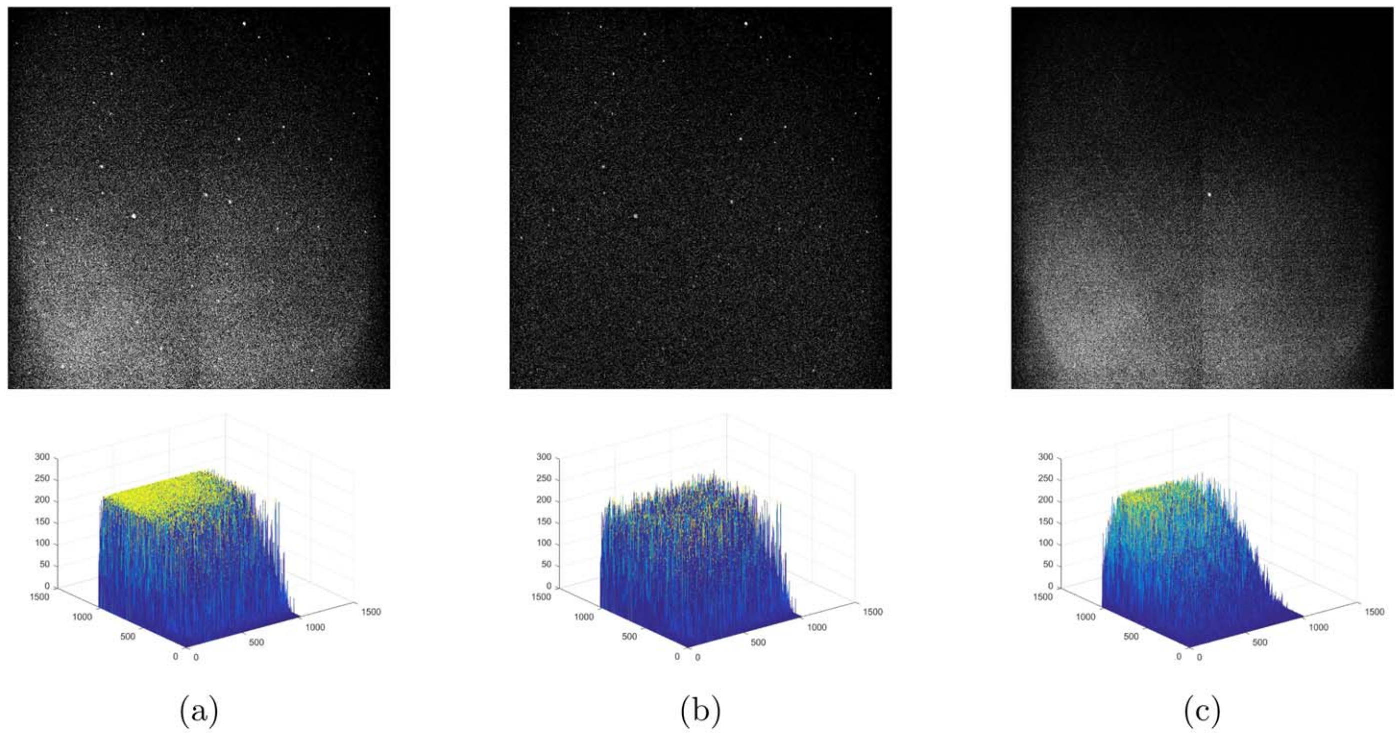

Figure 2. Image after the first stage processing. (a) Original image. (b) Background image. (c) Image after denoising and median. The corresponding 3D image is at the bottom.

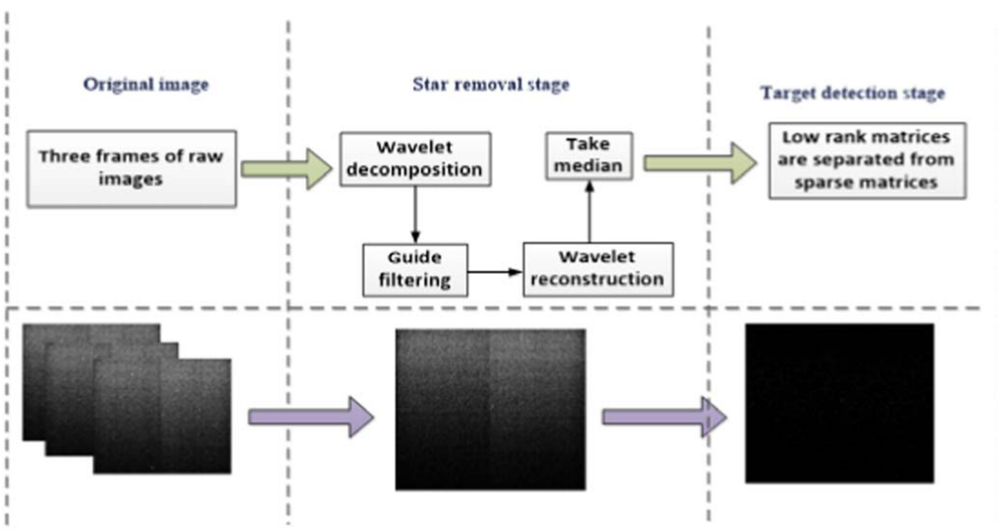

Figure 3. Structure diagram of space target extraction channel.

wavelet reconstruction. Since noise and space targets are mixed together, this step can suppress the influence of noise. We take the median of three consecutive images, and the main purpose of this operation is to remove stars. We will introduce in detail below.

The image processing method of wavelet transform can decompose the image signal into different subbands that are orthogonal to each other, which solves the problem that the image information of the traditional image pyramid is related to each other at different scales, and the wavelet transform method

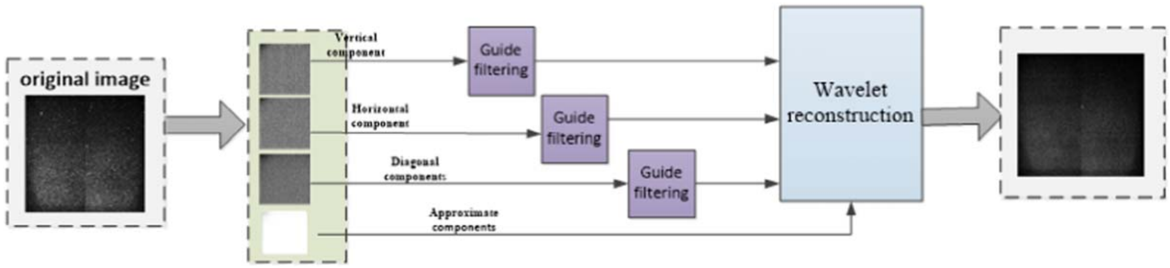

Figure 4. Star removal algorithm structure image.

can effectively simulate the human eye. The wavelet theory uses the multi-resolution decomposition ability to decompose the image into sub-images of different spaces and different frequencies, and then encodes the coefficients of the sub-images. At the same time, wavelet transform can better solve the contradiction between time and frequency resolution, so wavelet transform is very beneficial to the decomposition and reconstruction of image signals (Wang & Jiang 2019). We select the sym8 wavelet base to divide the image into different components, as shown in Figure 5 are the different components of the wavelet decomposition.

The original image $F(i)$ is first decomposed into high frequency components $G(i)$ and approximate components $X(i)$ by applying wavelet transform. The formula is:

$$F(i) = X(i) + G(i) = X(i) + N(i) + V(i) \tag{3}$$

The high frequency component $G(i)$ contains noise $N(i)$ and texture information $V(i)$. The high frequency component $G(i)$ can be expressed as:

$$G(i) = \{H_i, V_i, L_i\} \tag{4}$$

In the formula, H_i represents the horizontal component, V_i represents the vertical component, and L_i represents the diagonal component.

We apply wavelet transform to obtain the corresponding components of three consecutive images. To better preserve image edge details, we process each component using guided filtering. The algorithm not only exhibits better denoising performance. It can avoid the loss of fragmented information.

The guided filter has good edge preservation properties, which can remove noise on the basis of preserving edge details. The guided filter calculates the output image by considering the content of the guided image, and converts the edge structure of the guided image into the filter output. In the guided filtering step, when the input image and the guided image are the same, it can play the role of edge preservation (Wang & Jiang 2019). The filtering output image and the guiding image satisfy the local window linear relationship, and the filtering problem is transformed into an optimization problem with linear parameters. The definition formula is as follows:

$$q_i = a_k g_i + b_k, \quad \forall_i \in w_k \tag{5}$$

Among them, q represents the output image. g represents the guide image. a_k and b_k are the linear coefficients and offset coefficients in the window w_k , and w_k represents the window with a radius of h. This method assumes that q and g have a local linear relationship within a window centered at pixel k. Taking the derivative of Equation (5), the output will have edges only if the guide image has edges. In order to solve the coefficients a_k and b_k, assuming that p is the result of q before filtering, and satisfying to minimize the difference between q and p, according to the method of unconstrained image restoration, its value function is:

$$E(a_k, b_k) = \sum_{i \in w_k} ((a_k g_i + b_k - p_i)^2 + \varepsilon a_k^2) \tag{6}$$

Among them, ε is the regularization parameter. It can make a_k converge. P represents the input picture. Limit i in the window w, so that the value of a_k will not be too big. The coefficients a_k and b_k are respectively:

$$a_k = \frac{\frac{1}{|w|}\sum_{i \in w_k} p_i g_i - \overline{p_k} u_k}{\sigma_k^2 + \varepsilon} \tag{7}$$

$$b_k = \overline{p_k} - a_k u_k \tag{8}$$

Among them, u_k and σ_k^2 are the mean and variance of the guide image g in the window w_k, $\overline{p_k}$ is the mean of the input image p in the window w_K, and $|w|$ is the number of pixels in the window w_k.

Then we take the median of three consecutive images, which will eliminate the influence of stars. The star elimination stage algorithm prepares for subsequent algorithms. The hybrid denoising of wavelet transform and guided filtering can not only eliminate noise, but also greatly preserve the information of space targets. Figure 6(a) shows four images with different backgrounds. The noise, stars and targets are mixed together.

Figure 6(b) is the processed image, and the algorithm well removes stars and some noise. Figures 7(a) and (b) are respectively the pixel gray value distribution of Figures 6(a)

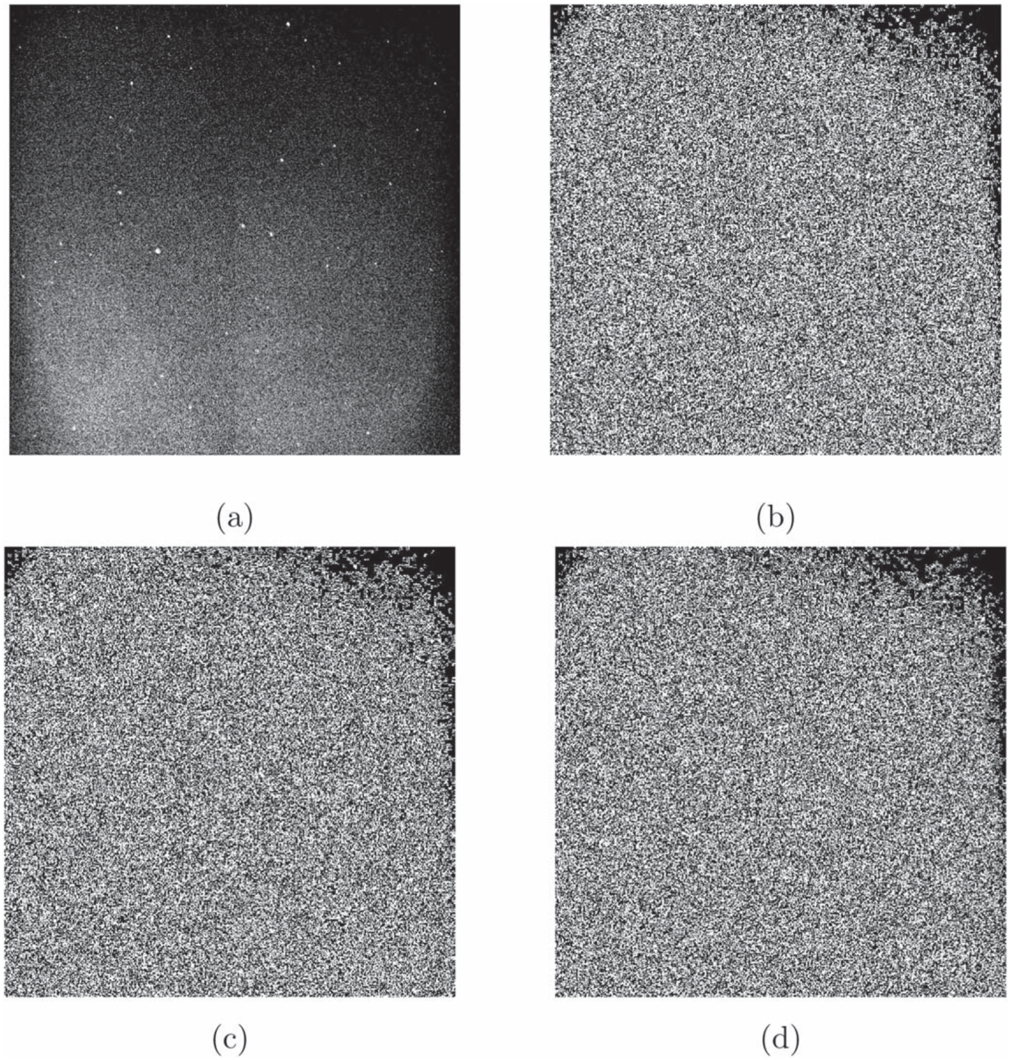

Figure 5. Wavelet decomposition: (a) Original image. (b) Vertical component. (c) Horizontal component. (d) Diagonal component.

and (b). From the intensity distribution diagram, it can be seen that the yellow dots represent stars or noise with high gray-scale intensity. After processing by our algorithm, the strong star points and noise are eliminated, and the noise is also weakened, which shows the effectiveness of the algorithm.

We consider the influence of the filter window size h of guided filtering on the experimental results. Here H represents the height of the image. Figure 8 is the result of using different window sizes. First, h cannot use a too small window size ($h = 0.1$ H), there will be residual noise, as shown in Figure 8(a). Also, h cannot be too large ($h = 0.5$ H or $h = 0.7$ H), as shown in Figures 8(b) and (c), it will obviously blur the image details. After many experiments, the regularization parameter is set to 0.04, the h parameter is set to 0.3H.

Experiment with several competitive algorithms, image differencing (ID) (Iwasawa et al. 1997), multiscale patch-based contrast measure (MPCM) (Wei et al. 2016), Local Contrast Method (LCM) (Chen et al. 2014), wavelet transformed (WT) (Boccignone et al. 1998) and our algorithm. The ID algorithm uses the parameter model of the background to approximate the pixel value of the background image, and then compares the background image and the sequence image differentially, the area with a large difference is the moving target area. MPCM method can change the contrast between the foreground target and the background, it is easier to separate small targets from the background using simple threshold segmentation. LCM method improves the contrast between the target and its neighbors to detect the target. WT algorithm utilizes the multi-scale analysis algorithm of wavelet to distinguish the

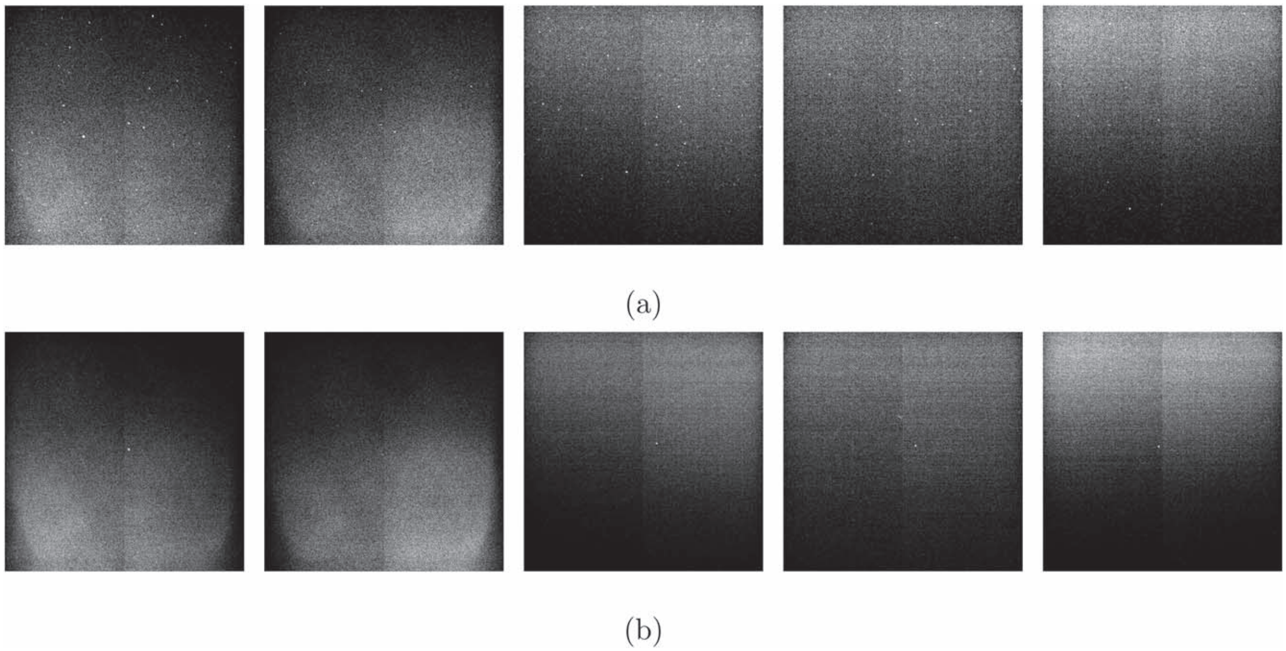

Figure 6. Five representative images and the results processed by our algorithm. (a) Original image. (b) The processing result of our method.

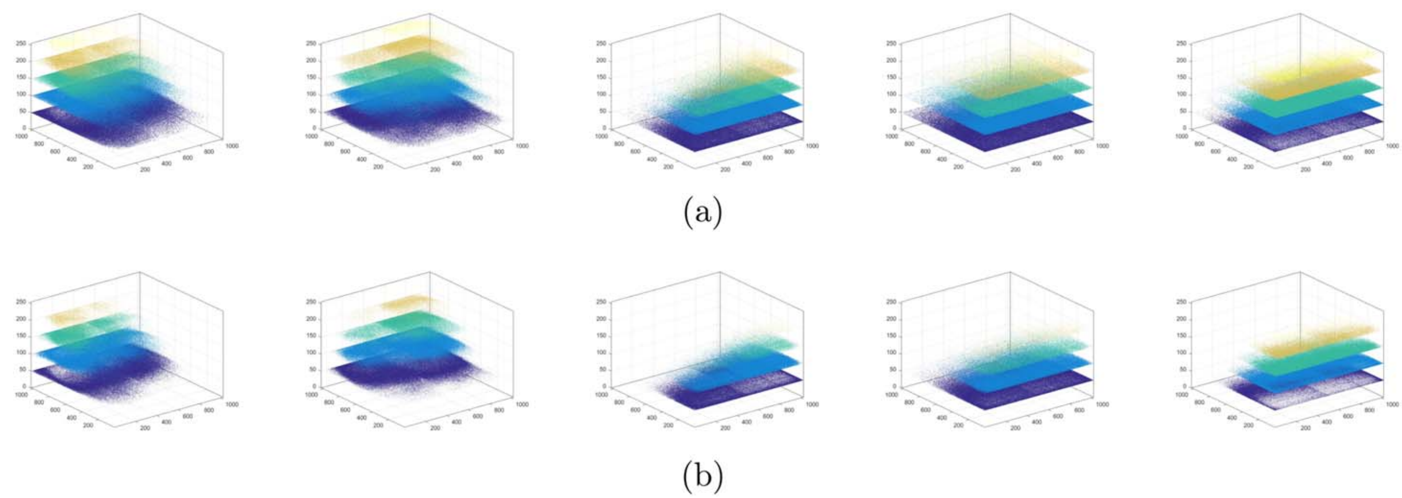

Figure 7. Pixel distribution of the corresponding image in Figure 6. (a) The grayscale distribution of the corresponding image in Figure 6(a), (b) shows the gray distribution image after processing.

background and the target. After the original image is subjected to discrete wavelet transform, image information of different frequency domain scales will be generated. Since the characteristic information of the target and background clutter is different in the frequency domain space of different scales, the target information is extracted. In our algorithm, the wavelet base of wavelet decomposition is sym8, the window of the guided filtering window is $h = 0.3$ H, and finally the median of three consecutive frames is taken. It can be seen from Figure 9 that the experimental results of ID and LCM algorithms are severely affected by noise, so the processing effect is not ideal. WT algorithm and MPCM algorithm have relatively good results, but they are still affected by stars. In general, our algorithm has achieved better results.

In order to further prove the effectiveness of the algorithm, this paper uses three indicators of local signal-to-noise ratio (LSNR) and gain signal-to-noise ratio (GSNR), and background suppression factor (BSF) for quantitative analysis. The

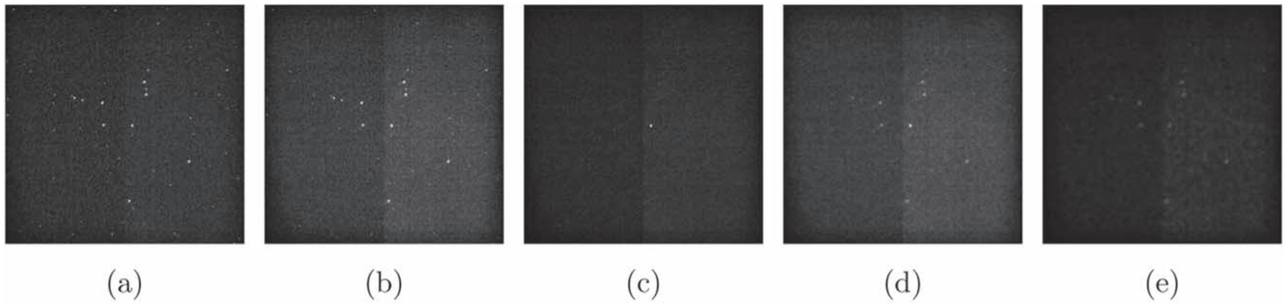

Figure 8. The algorithm selects different h value processing results. (a) Original image. (b) $h = 0.1$H. (c) $h = 0.3$H. (d) $h = 0.5$H. (e) $h = 0.7$H.

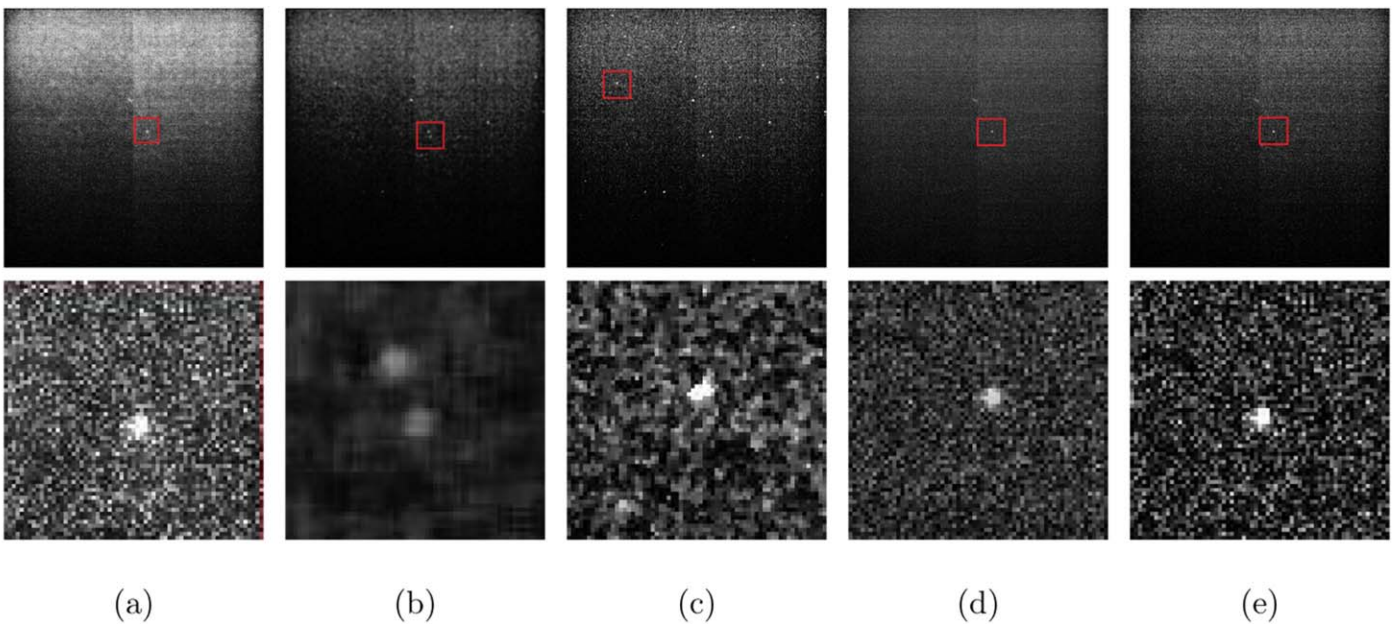

Figure 9. Comparison of background suppression effects of various algorithms: (a) ID. (b) MPCM. (c) LCM. (d) WT. (e) Ours.

definition of this indicator is as follows:

$$\mathrm{LSNR} = \frac{|I_{\max} - \mu_b|}{\sigma_b}$$
$$\mathrm{GSNR} = \frac{SNR_{\mathrm{out}}}{SNR_{\mathrm{in}}}$$
$$\mathrm{BSF} = \frac{\sigma_{\mathrm{in}}}{\sigma_{\mathrm{out}}} \tag{9}$$

In the formula, $I_{\max}$ represents the maximum pixel gray scale of the area where the target is located; μ_a and μ_b are the mean and standard deviation of the pixel gray scale within a certain scale neighborhood of the target, respectively; $\mathrm{SNR_{in}}$ represents the signal-to-noise ratio of the original image, and $\mathrm{SNR_{out}}$ represents the signal-to-noise ratio processed by our algorithm; σ_{in} and σ_{out} are the gray standard deviations of the original image and the global image processed by the algorithm. We use the first four images in Figure 6(a) as the original images and label them as scenario 1, scenario 2, scenario 3, and scenario 4. After processing with a variety of different algorithms, we calculate the LSNR, BSF and GSNR values, and the statistical results are shown in Table 1. According to formula (9), the larger the LSNR, the higher the signal-to-noise ratio of the target, and the easier it is to detect the target. The larger the GSNR, the stronger the algorithm ability to suppress background clutter and enhance the target, indicating that the algorithm performance is better. The larger the BSF value obtained by the algorithm, the better the effect of the algorithm in suppressing the complex background. Therefore, strong target enhancement capabilities and good background suppression capabilities are the keys to target segmentation.

The experimental results are shown in Table 1. The LSNR value of the original image is small. For different complex background images, each algorithm can improve the target

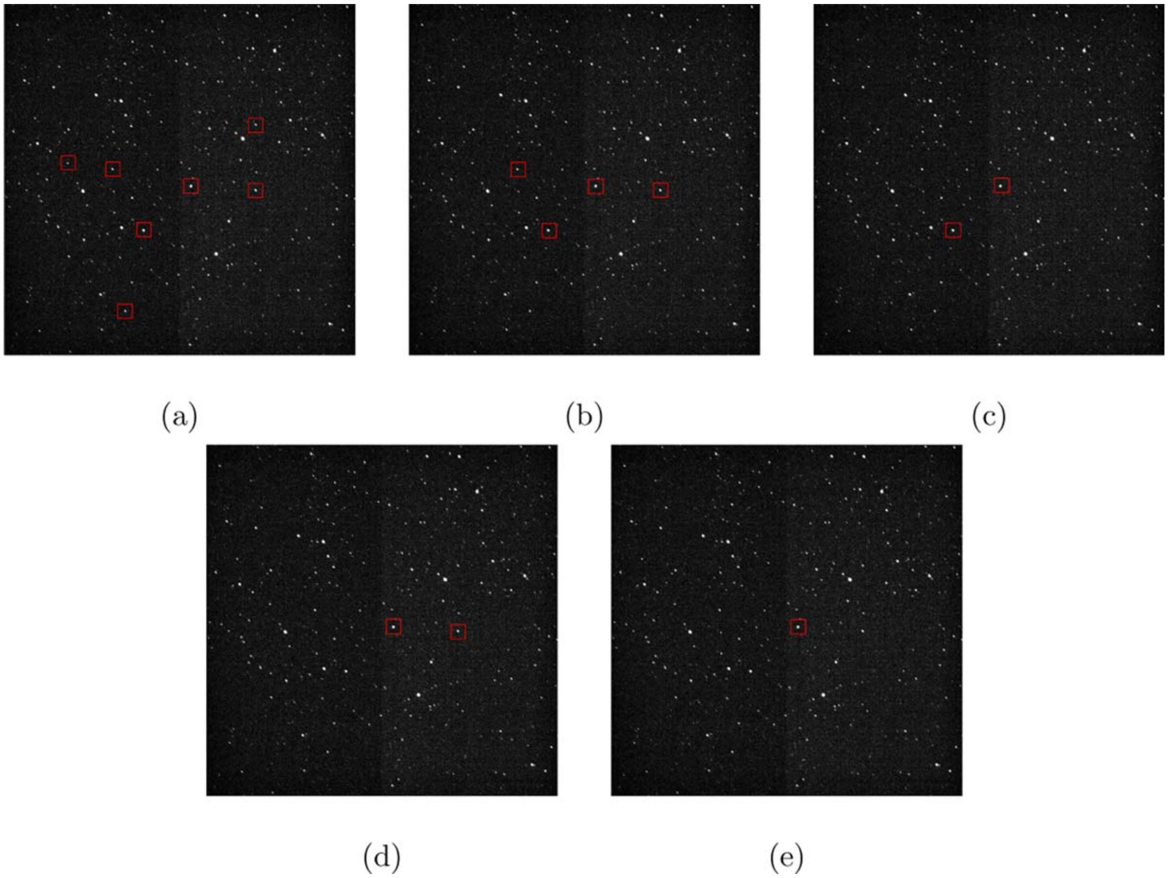

Figure 10. Comparison of processing results of several algorithms. (a) IMVP. (b) NTH.(c) HSS. (d) 1DSE. (e) Ours.

Table 1
The SNR, GSNR and BSF of Each Algorithm in Different Scenes (dB)

	Scenario 1			Scenario 2			Scenario 3			Scenario 4		
Algorithm	LSNR	GSNR	BSF	LSNR	GSNR	BSF	LSNR	GSNR	BSF	LSNR	GSNR	BSF
Original	2.706	…	…	2.543	…	…	1.316	…	…	3.572	…	…
ID	8.475	6.435	7.452	9.357	7.412	8.241	7.482	6.245	10.047	7.241	5.248	9.247
MPCM	16.237	8.972	3.247	14.253	11.243	8.634	14.721	12.341	7.658	15.249	13.257	8.325
LCM	7.159	5.247	4.286	8.142	6.347	7.524	9.247	8.146	6.324	5.237	4.219	6.301
WT	15.106	12.571	8.421	13.546	11.245	16.279	16.345	14.272	12.472	12.127	10.267	11.248
Ours	23.247	13.574	16.24	22.373	21.573	26.318	24.578	23.146	24.218	21.235	20.135	26.327

LSNR value to different degrees. For the four scenarios, the LSNR, GSNR, and BSF values obtained after processing by the ID, MPCM, and LCM algorithms are relatively small. The processing effect of the WT algorithm is relatively good, and our algorithm obtains the largest LSNR, GSNR and BSF values. Therefore, it shows that the algorithm in this paper can effectively suppress the background clutter and enhance the weak and small targets, which is beneficial to the subsequent threshold segmentation operation.

In order to fully illustrate the performance of the algorithm, the effect of the algorithm is more convincing. We have added several algorithms for comparative experiments. The algorithm mainly includes: NTH algorithm (Bai et al. 2009), IMVP algorithm (Yao et al. 2015), HSS algorithm (Du et al. 2016), 1DSE algorithm (Wei et al. 2018) and our algorithm. The experimental effect is shown in Figure 10. We can see that the IMVP algorithm is affected by the stars, and the detection result is less accurate. The detection effect of NTH algorithm, 1DSE

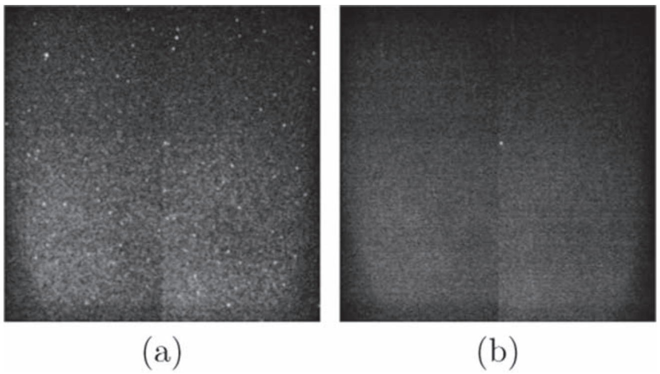

Figure 11. Image processed through the star removal stage. (a) Raw image. (b) Image processed through the star removal stage.

algorithm and HSS algorithm is ideal, but the algorithm is still affected by noise. Combined with the comparison images, our method achieves the best performance for the detection of space debris.

2.2. Target Detection Stage

The first stage mainly removes stars and some noise, so the processed image mainly includes noise, uneven background and targets. The background image is considered to be slowly changing, and the noise often presents a large area of continuous distribution in space (as shown in Figure 11(b)).

Even non-adjacent backgrounds in the image have a strong correlation, which makes them have a greater correlation in the gray-scale spatial distribution. This characteristic is widely present in astronomical images. We continue to study the properties of the image after being processed by the star removal stage, and the singular value curve of the image is given as shown in Figure 12. The singular values of the images are quickly reduced to 0, indicating that several images show low rank, and we use the formula to express as:

$$\mathrm{rank}(B) \leqslant K \tag{10}$$

K is a constant representing the complexity of the image.

In the actual star map, the visibility of the target is very low, and the local contrast is very low. Space target sizes vary from 2×2 to 10×10, the proportion of targets in the whole image is still small. Therefore, we treat it as a sparse matrix. In addition to this sparsity, no additional assumptions are made about the target image. The formula is expressed as:

$$\|T\|_0 < K \tag{11}$$

where $\|\cdot\|_0$ is the L0 norm of the number of non-zero entries in the calculation matrix. K is related to the target size. Obviously $K << X \times Y$ ($X \times Y$ is the size of the target). Based on the above analysis, the original image is decomposed by component analysis algorithm, and the target is searched in the decomposed sparse components.

$$D = T + B \tag{12}$$

Danelljan et al. proved that under the condition of matrix low-rank constraint, when the number of elements of matrix is $m \geqslant Cn6/5r \log n$, the matrix low-rank component recovery problem can be transformed into a convex optimization problem (Danelljan et al. 2014). Here C is a normal number, and r is the rank of the matrix. The convex optimization problem is expressed as follows:

$$\min_{M,B} rank(T) + \lambda \|B\|_0 \quad s.t. \quad D = T + B \tag{13}$$

Here $rank(\cdot)$ represents the rank function, $||B||_0$ represents the l_0 norm of matrix B, and λ is usually a constant greater than 0, which represents the weight. Since Equation (13) is an NP-hard problem (Hillar & Lim 2013), the objective function needs to be relaxed when solving. Since the envelope of the matrix rank is the kernel norm, and the convex hull of the matrix l_1 norm is the matrix l_1 norm, the above objective function can be relaxed as follows.

$$\min_{M,B} \|T\|_* + \lambda \|B\|_1 \quad s.t. \quad D = T + B \tag{14}$$

In the formula, $\|\cdot\|_*$ represents the matrix core norm, and $\|\cdot\|_1$ represents the l_1 norm of the matrix. There are many ways to solve this function. In the paper, we use the Accelerated Proximal Gradient (APG) algorithm to solve it (Ganesh et al. 2009).

The APG algorithm relaxes the equality constraint of Equation (14) into the objective function, and obtains the following Lagrangian function:

$$L(T, B, \mu) = \mu(\|T\|_* + \lambda \|B\|_1) + \frac{1}{2}\|D - T - B\|_F^2 \tag{15}$$

Below we give the pseudo program of the APG solving algorithm (where $\overline{\mu}$ is a positive number given in advance, $0\angle\eta\angle 1$). Finally, an adaptive segmentation method is adopted and refined to obtain the final detection results.

The pseudocode of the APG is Algorithm 1:

Algorithm 1. Accelerated Proximal Gradient algorithm pseudo program

Input: Input image D,λ, $\overline{\mu}$
Initialize: $k = 0$, Y_B^0, Y_T^0, B_0, T_0, t_0, μ_0
While not converged do
$B_{k+1} = D_{\mu_{k/L_f}}(Y_B^k + (D - Y_B^k - Y_T^k)/L_f)$
$T_{k+1} = S_{\mu_{k/L_f}}(Y_T^k + (D - Y_B^k - Y_T^k)/L_f)$
$t_{k+1} = (1 + \sqrt{1 + 4t_k^2})/2$
$Y_B^{k+1} = B_k + (t_k - 1)(B_k - B_{k+1})/t_{k+1}$
$Y_T^{k+1} = T_k + (t_k - 1)(T_k - T_{k+1})/t_{k+1}$
$\mu_{k+1} = \max(\eta\mu_k, \overline{\mu})$
Output:(B_k, T_k)

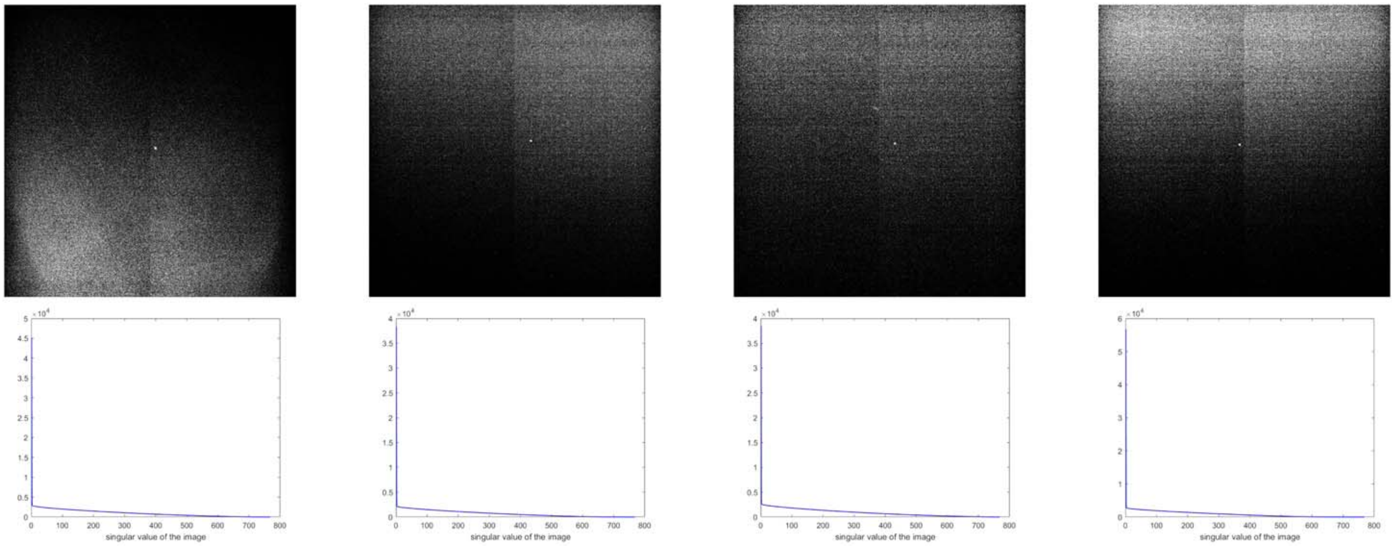

Figure 12. The low rank of the image. On the top are several representative astronomical images, on the bottom are the singular value curves.

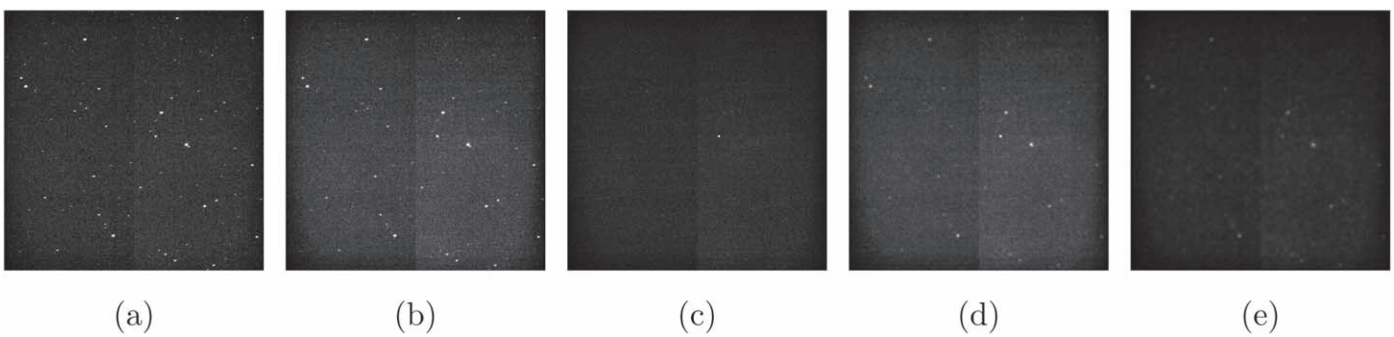

Figure 13. Experimental results of different λ values. (a) Original image. (b) $\lambda = 0.01$. (c) $\lambda = 0.03$. (d) $\lambda = 0.06$. (e) $\lambda = 0.09$.

Conducted multiple sets of experiments to explore the influence of λ value on the experiment. As shown in Figure 13, the experimental results of λ value of 0.01, 0.03, 0.06, and 0.09 are given. We can clearly see that when the value of λ is small ($\lambda = 0.01$), the algorithm regards noise as the target, which results in more residual noise in the experimental results (as shown in Figure 13(b)). When the λ value is 0.06 and 0.09, the experimental result will delete the target information by mistake (as shown in Figures 13(d) and (e)). Through a large number of experiments, we have found that when the value of λ is in the range of 0.03–0.05, the experimental results are ideal and most suitable for our observation system.

As shown in the Figure 14, the image is processed in two stages. As shown in Figure 14(b), the first stage removes the stars and part of the noise. After the second stage of processing, the algorithm detects the space target well (as shown in Figure 14(c)). The second row of Figure 14 corresponds to the 3D image, which we can see more clearly from the 3D image.

We conducted multiple sets of comparative experiments, the algorithm mainly includes: NTH algorithm, IMVP algorithm, HSS algorithm, 1DSE algorithm and our algorithm. We use the default setting for the comparison algorithm, and we will still adopt the parameter setting of wavelet base as sym8 and $\lambda = 0.03$ in our algorithm. Figures 15 and 16 are the algorithm comparison image and algorithm evaluation index curve. From Figures 15 and 16(a), we can see that the IMVP and NTH algorithms are affected by noise and stars, and their detection results have low accuracy. The 1DSE algorithm has a better detection effect, but it can be seen from the time running histogram in Figure 16(b) that this method takes a long time to calculate, and there is a problem of a large amount of calculation. The HSS algorithm has achieved relatively good detection results when the running time is short, but the algorithm will still be affected by noise. Combining the image comparison image in Figure 15 and the curve comparison

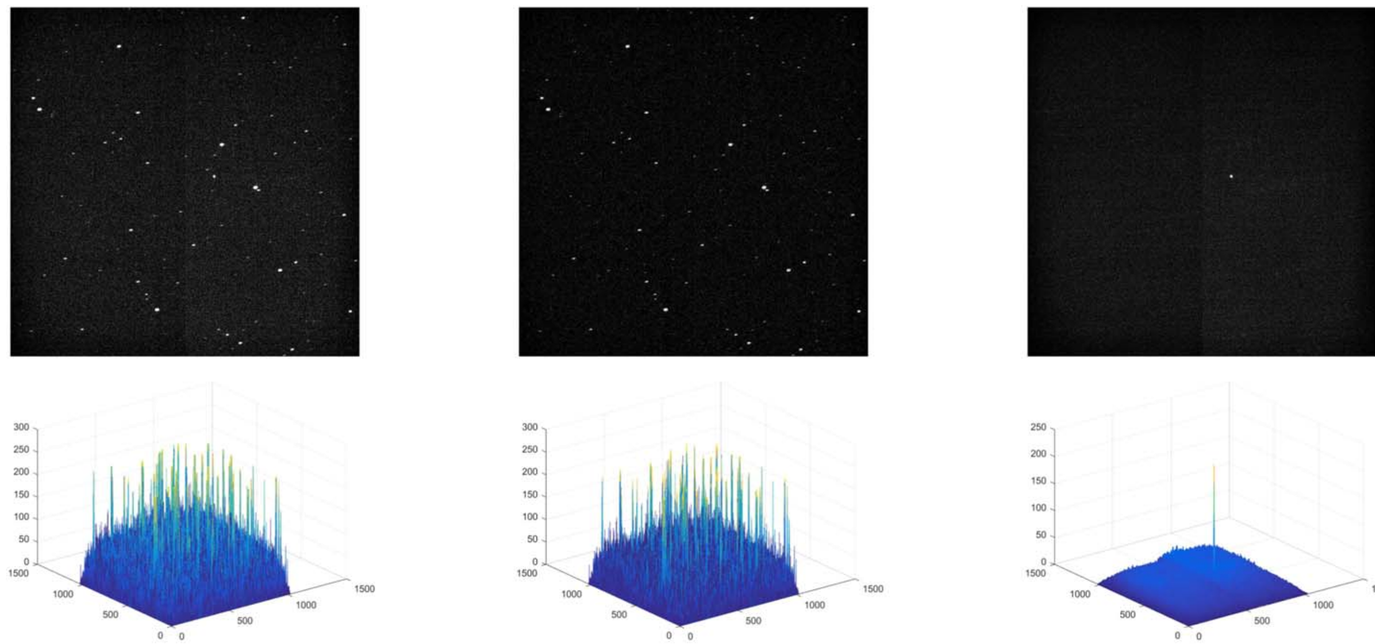

(a) (b) (c)

Figure 14. Real astronomical image processing effects. Top: (a) Original astronomical images. (b) The effect comparison image after the first stage processing. (c) The effect comparison image after the second stage processing. Bottom: 3D image of the corresponding image.

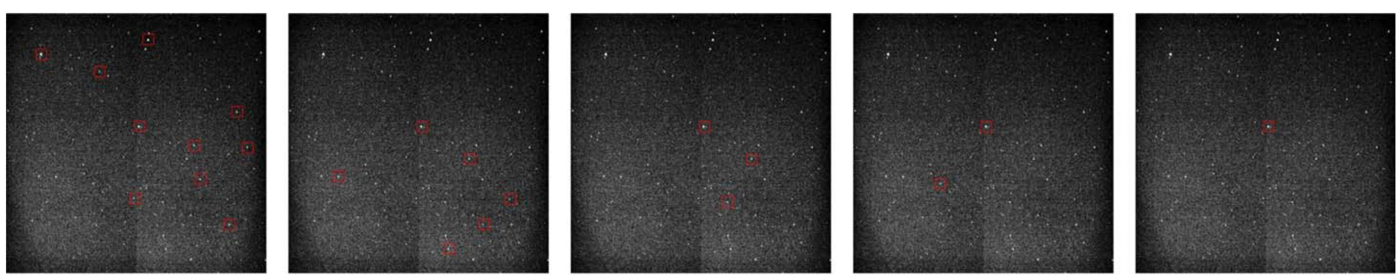

(a) (b) (c) (d) (e)

Figure 15. Comparison of processing results of several algorithms. (a) IMVP. (b) NTH. (c) HSS. (d) 1DSE. (e) Ours.

image in Figure 16, our method achieves the best performance for all space target detection.

3. Experiment

In order to evaluate the performance of our algorithm in detection and false alarm suppression, the algorithm was further tested on 500 real image sequences collected by astronomical telescopes. The diameter of the telescope is 15 cm, and the telescope field of view is $2\overset{\circ}{.}5 \times 2\overset{\circ}{.}5$, the telescope is in the target tracking mode, and the image size is 4096×4096 pixels. Therefore, under short exposure conditions, there is no difference between the shape of the target and the star, and the image contains a lot of noise, so the detection of target is a difficult task. In this section, we conduct quantitative and qualitative analysis through a large number of experiments to illustrate the performance of the algorithm in this paper.

3.1. Real Astronomical Image Detection Experiment

We use two types of algorithms for experimental comparison, one is the same type of space target detection algorithm, and the other is the background suppression algorithm. The effect of the algorithm is more fully explained, which makes the experimental results more convincing. For the same type of

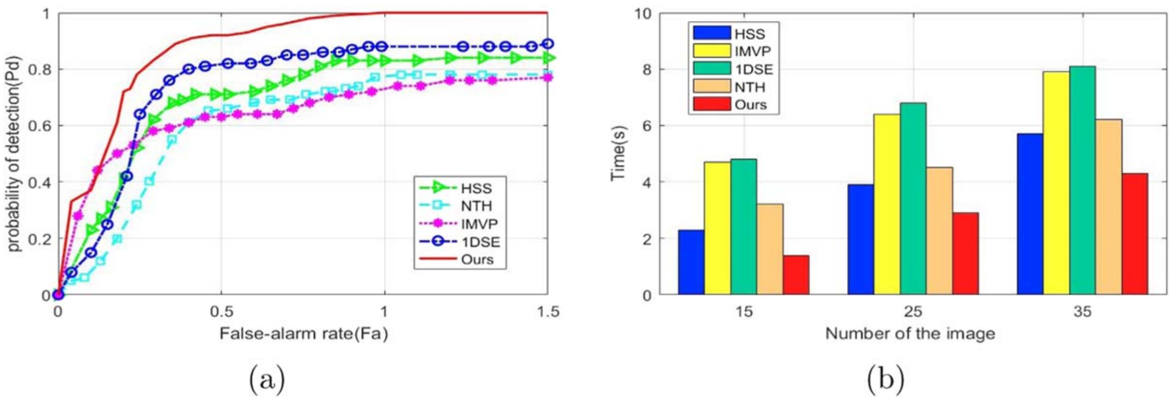

Figure 16. Performance curve of multiple algorithms. (a) Pd–Fa curve of multiple algorithms. (b) Running time curve of multiple algorithms.

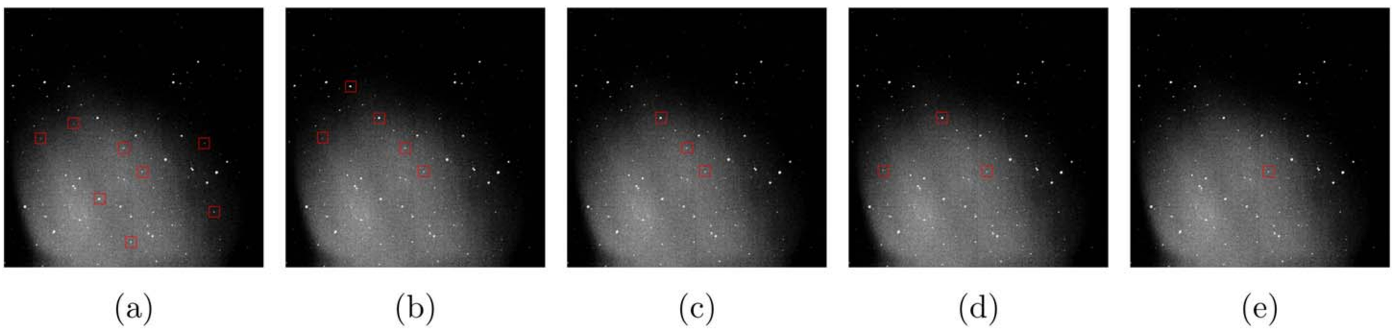

Figure 17. Comparison of processing results of several algorithms. (a) IMVP. (b) NTH. (c) HSS. (d) 1DSE. (e) Ours.

Table 2
Details of Five Real Image Sequences

No.	Background Description	Target Description
1	• A lot of star points and noise, the star is slightly tailed	• The target is dim and the target changes to a certain extent
2	• A lot of star points and noise, the star is slightly tailed	• Bright space targets
3	• There are fewer stars, heavy noise	• Small dim space target
4	• There are more stars, the star is slightly tailed	• Small dim space target
5	• There are fewer stars, heavy noise	• The target is dim and the target changes to a certain extent

algorithm, we still use NTH algorithm, IMVP algorithm, HSS algorithm, 1DSE algorithm and our algorithm for experimental comparison. The results are shown in Figure 17. It can be clearly seen from the experimental comparison results that the IMVP and NTH algorithms are affected by noise and stars, and there are many wrong identifications in the detection results. The experimental results of HSS and 1DSE algorithms have less influence on noise, but there will still be false detections in scenes with many stars. From a comprehensive comparison, our algorithm achieves ideal detection results and can completely detect space debris targets.

In order to verify the advantages of the proposed method, tophat algorithm (Zhou et al. 2014), TDLMS algorithm (Hadhoud & Thomas 1988), maxmean algorithm and maxmedian algorithm (Deshpande et al. 1999), are used as the benchmark algorithm to detect the same five image sequences. The detailed description of the five images is given in Table 2. We set the structuring elements of the tophat algorithm to be 5×5. The filtering window of maxmean and maxmedian algorithms is 8×8. The wavelet base of wavelet decomposition in our algorithm is sym8, $\lambda = 0.03$, and the detection result is shown in Figure 18. The second column of Figure 18 is the background image estimated by our algorithm. This can help us

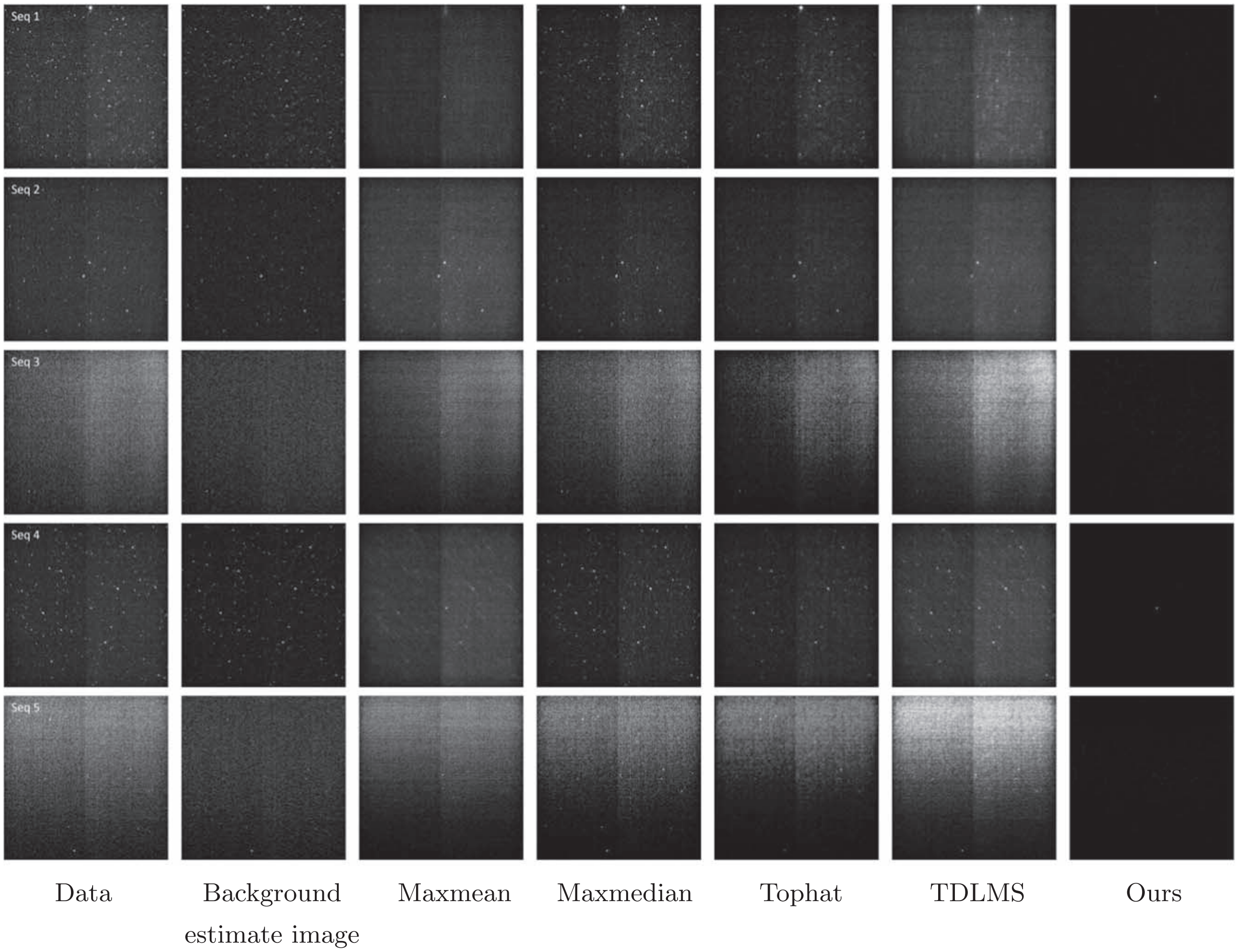

Figure 18. The results of processing by different algorithms.

better improve the accuracy of space target detection, which is of great significance to the subsequent star map matching algorithm. The third to seventh columns in Figure 18 are the detection results of the five algorithms. When the target is dark and weak, the processing effect of the maxmean algorithm is not ideal, but when the target is bright, the result obtained is relatively good. The maxmedian and tophat algorithms also have the problem of high false detection rate when the target is dimly weak. The TDLMS algorithm has a poor detection effect on astronomical images with complex background and many noise points.

The first column of Figure 18 is the original image, which is marked as Seq 1–5 in order from top to bottom. The data selected can be roughly divided into two categories: Seq 2, Seq 3 and Seq 5 images have a lot of noise and stars in the background. Seq 1 and Seq 4 are slightly prolonged when the exposure time is increased. Our algorithm achieves better detection results in both cases. The overall performance of our algorithm is the best, while the background is effectively suppressed, the noise is also effectively suppressed, and the algorithm does not lose effective target information. Figure 19 shows the precision-recall curve of the detection results. Our algorithm outperforms the other four benchmark algorithms. Figures 20(a) and (b) are the BSF curves and algorithm running time histograms obtained by several algorithms. It can be clearly seen from the curves that the tophat algorithm obtains a lower BSF value and a longer running time. In general, the BSF value obtained by our algorithm maintains a high level, and the running time is the least, which shows the effectiveness of the algorithm.

4. Conclusion

We propose a faint space debris detection algorithm based on small aperture telescopes. We establish a new image observation model. The model is mainly divided into two

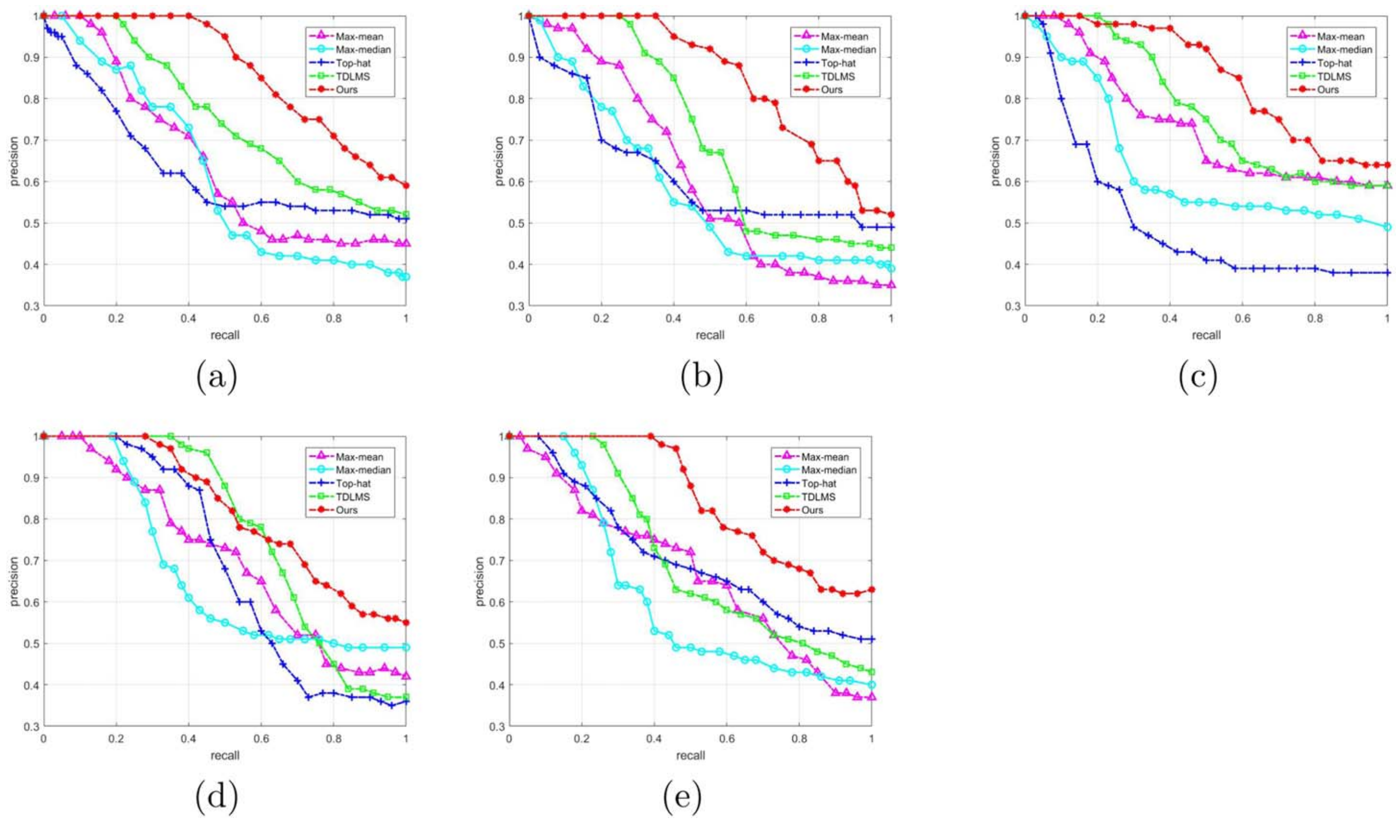

Figure 19. Curve analysis of five image sequence processing results. (a) Seq 1. (b) Seq 2. (c) Seq 3. (d) Seq 4. (e) Seq 5.

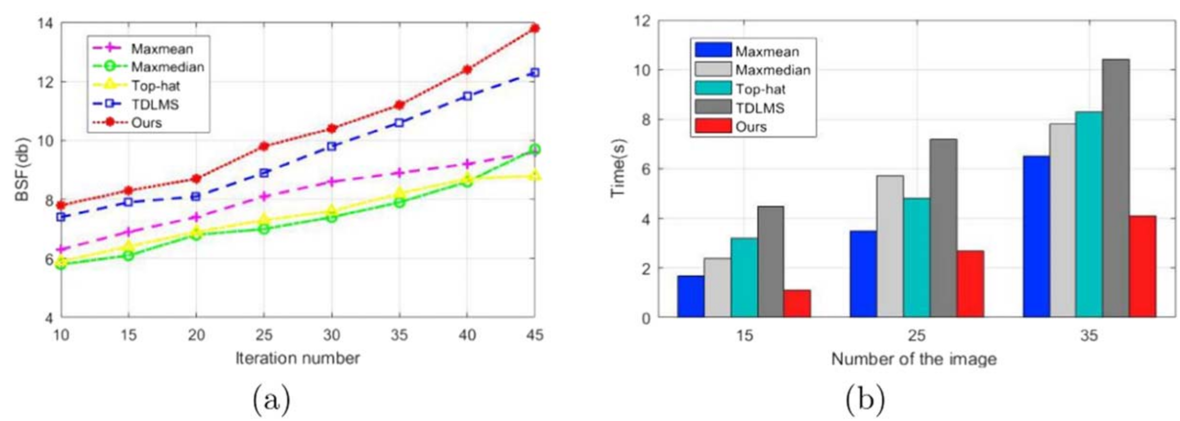

Figure 20. Performance curve of multiple algorithms. (a) BSF curves for various algorithms. (b) Running time curve of multiple algorithms.

stages for analysis. In the first stage, we use a filtering method that combines wavelet decomposition and guided filtering to suppress a large number of star points in the image background. In the second stage, the target matrix and the background matrix are regarded as a sparse matrix and a low-rank matrix, and the final goal is to obtain the target matrix. In the next step, we will use the algorithm for asteroid detection or other similar applications. In addition, we will explore other applications of the algorithm.

Acknowledgement

The research work was supported in part by the National Natural Science Foundation of China (NSFC) (U2031129 and

12003052), and Youth Innovation Promotion Association of the Chinese Academy of Sciences (2018079).

References

Bai, X., Zhou, F., & Xie, Y. 2009, SigPr, 89, 1973
Boccignone, G., Chianese, A., & Picariello, A. 1998, ICPR, 2, 1776
Castronuovo, M. M. 2011, AcAau, 69, 848
Chen, C. L., Li, H., & Wei, Y. 2014, IEEE T Geosci Remote, 52, 574
Du, B., Zhang, Y. X., & Zhang, L. P. 2016, ITIP, 25, 5345
Danelljan, M., Khan, F. S., & Felsberg, M. 2014, CVPR, 143, 1090
Deshpande, S., Er, M., & Ronda, V. 1999, Proc. SPIE, 3809, 74
Ganesh, A., Wright, J., & Ma, Y. 2009, CAMSAP, 3, 213
Hadhoud, M. M., & Thomas, D. W. 1988, ITCS, 35, 485
Hillar, C. J., & Lim, L. H. 2013, J. ACM, 60, 45
Iwasawa, S., Ebihara, K., & Ohya, J. 1997, CVPR, 15
Jia, P., Liu, Q., & Sun, Y. 2020, AJ, 159, 212
Jiao, J., & Lingda, W. 2017, in Proc. 2nd Int. Conf. on Image, Vision and Computing (ICIVC) (Chengdu: IEEE), 53
Liu, R., Lu, Y., & Gong, C. 2012, InPhT, 55, 380
Murphy, T. S., Holzinger, M. J., & Flewelling, B. 2016, JGCD, 40, 497
Nunez, J., Nunez, A., & Montojo, F. J. 2015, AdSpR, 56, 218
Schildknecht, T. 2007, A&ARv, 14, 41
Sun, R. Y., & Zhao, C. Y. 2013, RAA, 13, 604
Sun, R. Y., Zhan, J. W., & Zhao, C. Y. 2015, ActaAstro, 110, 9
Schildknecht, T., Musci, R., & Ploner, M. 2004, AdSpR, 34, 901
Sun, Q., Niu, Z., & Wang, W. 2019, Senso, 19, 4026
Wei, M. S., Xing, F., & You, Z. 2018, LSA, 7, 97
Wang, E. D., & Jiang, P. 2019, Appl Surf Sci, 9, 1
Wang, X. Y., Peng, Z. M., & Zhang, P. 2017, IEEE Geosci. Remote Sens. Lett., 14, 1700
Wei, Y. T., You, X., & Li, H. 2016, PatRe, 58, 216
Xi, J. B., Wen, D. S., & Song, Z. X. 2015, JICS, 12, 161
Yanagisawa, T., Kurosaki, H., & Banno, H. 2012, in Proc. Advanced Maui Optical and Space Surveil-lance Technologies Conf., 1114, 9197
Yao, D., Wen, D., & Xue, J. 2015, Image Process. Anal, 9675, 96752
Zhou, J., Lv, H., & Zhou, F. 2014, in Int. Symp. on Optoelectronic Technology and Application, 93011L